AGU PUBLICATIONS

JGR

Journal of Geophysical Research: Solid Earth

RESEARCH ARTICLE
10.1002/2014JB011797

Fractal degassing from Erebus and Mayon volcanoes revealed by a new method to monitor H_2O emission cycles

Társilo Girona[1], **Fidel Costa**[1], **Benoit Taisne**[1], **Brian Aggangan**[2], and **Sorvigenaleon Ildefonso**[1]

[1]Earth Observatory of Singapore, Nanyang Technological University, Singapore, [2]Philippine Institute of Volcanology and Seismology, Quezon City, Philippines

Key Points:

- A new method to monitor the emission cycles of volcanic water vapor
- The frequency spectra of H_2O time series are fractal
- H_2O and SO_2 time series can have different spectral content

Supporting Information:

- Table S1

Correspondence to:
T. Girona,
tarsilo.girona@gmail.com

Citation:
Girona, T., F. Costa, B. Taisne, B. Aggangan, and S. Ildefonso (2015), Fractal degassing from Erebus and Mayon volcanoes revealed by a new method to monitor H_2O emission cycles, *J. Geophys. Res. Solid Earth*, *120*, doi:10.1002/2014JB011797.

Received 23 NOV 2014
Accepted 5 APR 2015
Accepted article online 8 APR 2015

Abstract Many active volcanoes around the world release passively large amounts of gas between eruptions. Monitoring how these gas emissions fluctuate over time is crucial to infer the physical processes occurring within volcanic conduits and reservoirs. Here we report a new method to capture remotely the spectral properties of the emissions of H_2O, the major component of most volcanic plumes. The method is based on a new theoretical model that correlates the volcanogenic water content of condensed volcanic plumes with the intensity of the light scattered by the droplets moving with the gas. In turn, we show that light intensity of the plume, and thus steam pulses time series, can be obtained with a proper analysis of digital images. The model is experimentally validated by generating condensed plumes with an ultrasonic humidifier, and then the method is applied to the gas plumes of Erebus and Mayon volcanoes. Our analysis reveals three main features: (1) H_2O time series are composed of numerous periodic components of finite duration; (2) some periodic components are common in H_2O and SO_2 time series, but others are not; and (3) the frequency spectra of the H_2O emissions follow a well-defined fractal distribution, that is, amplitude (Δ) and frequency (ν) are correlated by means of power laws ($\Delta \propto \nu^{\gamma}$), with exponent $\gamma \approx -1$ for Erebus and for Mayon. These findings suggest that quiescent degassing emerges from the complex coupling between different processes occurring within magma plumbing systems. Our method is ideal for real-time monitoring of high-frequency H_2O cycles at active volcanoes.

1. Introduction

Monitoring degassing cycles and gas puffing at active volcanoes is valuable for volcanic surveillance because they are a proxy for the physical processes occurring within magma conduits and reservoirs [e.g., *Ripepe et al.*, 2002; *Allard et al.*, 2005; *Tamburello et al.*, 2012]. Degassing cycles are currently monitored using remote methods as they allow obtaining time series at high sampling rates and are safer than in situ direct collection of volcanic gases [*McGonigle and Oppenheimer*, 2003]. For instance, *Harris and Ripepe* [2007] and *Branan et al.* [2008] analyzed gas puffing activity at Stromboli and Masaya by measuring temperature changes of the vent with thermal infrared thermometers and thermal imagers; *Oppenheimer et al.* [2009] and *Boichu et al.* [2010] registered SO_2 cycles at Erebus volcano with spectroscopic techniques, and more recently, *Tamburello et al.* [2013] monitored SO_2 pulsations at Etna with UV cameras.

Despite the variety of information that can be obtained from the different remote sensing techniques to monitor degassing cycles and gas puffing, none of them can actually capture the spectral properties of the H_2O emissions, which is by far the major component of most volcanic plumes [e.g., *Symonds et al.*, 1994; *Shinohara*, 2008]. This is mostly due to the difficulty of monitoring the water content of volcanic plumes, which is typically done by measuring simultaneously the SO_2 concentration with ultraviolet absorption spectrometers or UV cameras, and the molar ratio $[H_2O]/[SO_2]$ with OP-FTIR (open-path Fourier transform infrared) spectrometers [e.g., *Burton et al.*, 2000; *Oppenheimer and Kyle*, 2008; *Aiuppa et al.*, 2008]. An added limitation is that OP-FTIR technique can only supply reliable information when the spectrometer and an infrared lamp can be installed at opposite sides of the volcanic crater rim, since only close to the gas plume, the infrared radiation absorbed by atmospheric water vapor is minimized [e.g., *Burton et al.*, 2000; *McGonigle and Oppenheimer*, 2003; *Sawyer et al.*, 2011]. Here we aim to alleviate these difficulties and limitations by reporting a complementary method that allows monitoring H_2O pulsations from several kilometers afar from the plume. Contrary to the above-mentioned OP-FTIR technique, whose measurement principle is the absorption of radiation by H_2O molecules, the method we propose is based on the light scattered by the micrometric water droplets that travel with the gas of condensed volcanic clouds. This approach allows us to capture the spectral features of the H_2O emissions because the brightness of condensed plumes increases at each steam pulse, a fact that has been previously highlighted but not fully exploited [e.g., *Matsushima and Shinohara*, 2006; *Harris and Ripepe*, 2007].

In the next sections, we first introduce a new theoretical model that correlates the brightness of condensed volcanic plumes with the water vapor emissions. We also show how to obtain a brightness time series with commercial digital cameras, and then, we validate the fundamentals of the model by performing some laboratory experiments. Later, we explain how to process a digital brightness time series, and we apply the method to capture for the first time the spectral properties of the steam emissions from Erebus and Mayon volcanoes. Finally, we discuss our results and the limitations of the method.

2. Theoretical Model

The methodology we propose to track steam emission cycles applies to condensed volcanic clouds, which are commonly seen at active volcanoes during quiescence under many atmospheric conditions [*Matsushima*, 2005; *Matsushima and Shinohara*, 2006]. Volcanic clouds form when the hot volcanic gases (with temperatures of a few hundred degrees) leave the vent and quickly mix with the surrounding air, thus forming a saturated cooler mixture of volcanogenic water vapor, other less abundant volcanic gases (mostly CO_2 and SO_2), water vapor and dry air from the atmosphere, and micrometric water droplets [e.g., *Gassó*, 2008]. Water droplets, which are very light and hence travel with the gas plume, act as secondary source of radiation by scattering the sunlight [e.g., *Bohren and Huffman*, 2004]. Therefore, the time-dependant luminance $I(t)$ received by a digital optical sensor pointing toward the volcanic gas plume can be written as:

$$I(t) = I_N(t) + I_b(t) \tag{1}$$

where $I_N(t)$ is the luminance of the radiation scattered by N water droplets of equal size and $I_b(t)$ is the luminance corresponding to the background radiation, which is the radiation coming from the crater rocks and/or from the sky (whatever is behind the plume). A similar approach has been used to track turbulence in seeded flows and is valid as long as the concentration of water droplets in the cloud is not high enough to absorb the background radiation [*Roehle et al.*, 2000; *Findeisen et al.*, 2005; *Terhaar and Paschereit*, 2012]. The term $I_N(t)$ can be written at first-order approximation as [e.g., *Bohren and Huffman*, 2004]:

$$I_N(t) = N(t)\ f(t) \tag{2}$$

where we take into account that the number of water droplets $N(t)$ change with time due to the gas-puffing activity or due to atmospheric changes of relative humidity, pressure, or temperature [*Matsushima and Shinohara*, 2006]. The term $f(t)$ is the luminance scattered by a single water droplet, and it can be written according to Mie theory as a function of the luminance of the incident radiation (sunlight), the diameter of the droplet, the refraction index of water, the distance from the droplets to the observation point, and the angle formed by Sun-plume-observer [e.g., *Lock and Yang*, 1991; *Hergert and Wriedt*, 2012]. Note that the direct radiation coming from the Sun is considered larger than the diffuse radiation coming from the sky. Therefore, $f(t)$ varies with time depending on the position of the Sun along the day. By using equation (2), we assume single scattering, that is, the radiation scattered by the volcanic cloud is the sum of the radiation scattered by each water droplet, which is satisfied as long as the concentration of droplets is low enough [e.g., *Bohren and Huffman*, 2004].

The number of water droplets inside a given region of condensed plume $N(t)$ can be written in terms of the mass of volcanic water contained in that region $m_v(t)$. From mass conservation, we can state that the mass of volcanic water ($m_v(t)$) plus the mass of atmospheric water ($m_a(t)$) equals the mass of saturated water vapor ($m^s_{\text{vap}}(t)$) plus the mass of liquid water ($m_{\text{liq}}(t)$) from the droplets. In turn, the mass of liquid water is related to the number of droplets through $m_{\text{liq}}(t) = \hat{m}_d N(t)$, $\hat{m}_d$ being the mass of a droplet of average size, whereas the mass of atmospheric water is related to the mass of volcanic water through $m_a(t) = r(t)q(t)m_v(t)$, $r(t)$ being the mixing ratio between the mass of air and the mass of volcanic gases, and $q(t)$ the specific humidity of the atmosphere (mass of water vapor per unit mass of air) at crater levels. Hence, the number of water droplets within a region of the plume at a given time can be written after rearranging terms as:

$$N(t) = \frac{1 + r(t)q(t)}{\hat{m}_d} m_v(t) - \frac{m^s_{\mathrm{vap}}(t)}{\hat{m}_d} \tag{3}$$

By combining equations (1)–(3), we can write the luminance *I*(*t*) emitted from a given region of the plume as:

$$I(t) = \left[\frac{1 + r(t)q(t)}{\hat{m}_d} f(t)\right] m_v(t) \;\; + \left[I_b(t) - \frac{m^s_{\mathrm{vap}}(t)}{\hat{m}_d} f(t)\right] \tag{4}$$

This equation shows that the luminance *I*(*t*) of the plume can be used to monitor water vapor cycles $m_v(t)$ if the temporal variability of the other parameters is known and corrected. On the other hand, we propose to monitor the luminance *I*(*t*) simply by calculating the brightness of digital images $I_d(t)$. These two parameters are proportional ($I_d(t) = \alpha I(t)$) if a gamma correction is not applied to the image (an operation that compensates some properties of human vision) and for a given shutter speed and aperture of the camera [*Wüller and Gabele*, 2007]. Therefore, equation (4) can be written as:

$$I_d(t) = a(t)\, m_v(t) + \, b(t) \tag{5}$$

where $a(t) = \alpha f(t)[1 + r(t)q(t)]/\hat{m}_d$ and $b(t) = \alpha\left[I_b(t) - m^s_{\mathrm{vap}}(t) f(t)/\hat{m}_d\right]$. In turn, the digital brightness of a given region of interest $I_d(t)$ can be calculated using the following approximation [e.g., *Bala and Braun*, 2004]:

$$I_d(t) = \sum_i I_{i,d}(t) = \sum_i [0.2989\, R_i(t) + 0.5870\, G_i(t) + 0.1140\, B_i(t)] \tag{6}$$

where $I_{i,d}(t)$ is the digital brightness of each pixel *i* of the region of interest, which is measured in digital units (DUs) and varies between 0 (completely black) and 255 (completely white). The factors $R_i(t)$, $G_i(t)$, and $B_i(t)$ are the digital values of red, green, and blue color in RGB color space. Indeed, equation (6) represents a transformation of the image from RGB color space to gray scale by conserving the luminance [e.g., *Bala and Braun*, 2004].

3. Validation of the Linear Correlation Between Digital Brightness and Steam Emissions

Our model suggests that steam emission time series $m_v(t)$ can be obtained indirectly by calculating the digital brightness $I_d(t)$ of the condensed plume with a sequence of images and then correcting by the time variability of the terms *a*(*t*) and *b*(*t*) of equation (5). Below, we validate the linear correlation between $I_d(t)$ and $m_v(t)$ by performing experiments with an ultrasonic humidifier. Then, we show up to which extent our experimental results apply to actual volcanic plumes.

3.1. Experiments With Condensed Plumes

Equation (5) shows a linear relation between the brightness of a digital image I_d and the mass of volcanic water within a region of the condensed plume m_v. To validate this relation, we generated a condensed cloud with an ultrasonic humidifier (model Executive Standard, GB4706.48-2000, supplied by Bringnew Pte. Ltd., Singapore). Ultrasonic humidifiers are based on the principle of atomization by high-frequency mechanical oscillations, which are induced by a piezoelectric transducer submerged in a water tank and excited with a periodic MHz signal (Figure 1a). When the ultrasonic waves reach the water level, a fine mist of water droplets with a narrow size distribution ranging between 1 and 5 μm (on the same order of magnitude than water droplets within volcanic clouds formed immediately downwind the volcano [e.g., *Gassó*, 2008]) is atomized due to a combination of cavitation and capillary effects [e.g., *Lozano et al*., 2003]. These small droplets evaporate adiabatically by increasing the relative humidity of the air within the tank until it becomes saturated and forms a cloud. This cloud is then released from the tank through an opening, which was connected to a 35 cm long chimney with inner diameter of 19 mm that ended with a nozzle of inner diameter equal to 15 mm.

The humidifier was placed on a weighing scale to measure the weight variations with time, from which we calculated the atomization rate *Q* (kilogram of water released per second). Different atomization rates can be chosen by changing the voltage supplied to the piezoelectric transducer and thus by varying the

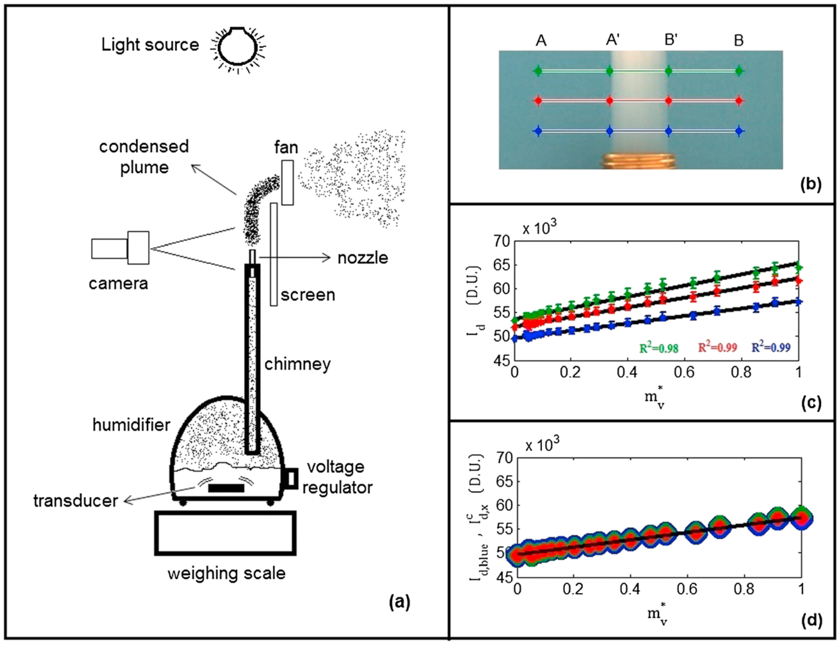

Figure 1. Experimental setup and results. (a) Sketch of our experimental setup. An ultrasonic humidifier atomizes micrometric water droplets by means of high-frequency mechanical oscillations generated with a piezoelectric transducer. A droplet cloud, emulating a condensed volcanic plume, is released through a vertical chimney. The stream of water droplets is stabilized with a fan and recorded with an IP camera. (b) Example of the images we recorded in our experiments. This image corresponds to an atomization rate of $Q = 44.4 \pm 0.2$ mg/s. The green, red, and blue lines correspond to the three sections we analyze. Segments *AB* and *A′B′* are used for analysis and correction of the brightness time series (see text for details). (c) Digital brightness I_d in digital units (DUs) versus normalized mass of water m_v*. The green, red, and blue dots with error bars correspond to the measurements from the lines of the same color in Figure 1b. The best fit lines are $I_{d,\mathrm{green}} = (11,700{\pm}400)m_v^* + (53,710{\pm}180)$ for the green region, $I_{d,\mathrm{red}} = (10,000{\pm}200)m_v^* + (52,140{\pm}110)$ for the red region, and $I_{d,\mathrm{blue}} = (7740{\pm}160)m_v^* + (49,690{\pm}80)$ for the blue region. R^2 is the correlation coefficient. (d) Corrected digital brightness of the green and red lines $I_{d,x}^c$, and digital brightness of the blue line $I_{d,\mathrm{blue}}$, versus m_v*. These results confirm the linear correlation between the digital brightness of the condensed plume and the amount of water ejected by the humidifier.

amplitude of the ultrasonic waves [*Lozano et al.*, 2003]. In turn, the atomization rate can be written as $Q = C_v S v$, where C_v is the concentration of water coming out from the humidifier (kilogram of water—equivalent to m_v—per cubic meter of plume), S is the section of the plume, and v is the velocity of the stream of droplets. If we normalize the atomization rate (for example, with respect to the maximum atomization rate reached in our experiments), and the section and velocity of the plume are fixed, it is satisfied that $Q^* = C_v^* = m_v^*$, where the asterisk represents normalized values. Thus, different values of m_v^* (or m_v) can be obtained simply by choosing different atomization rates. Constant section and velocity are achieved in our experiments with a fan located above the nozzle that suctions and stabilizes the stream of droplets (Figure 1a).

The steady flux of droplets for a given atomization rate was recorded by taking 5000 images with an IP camera (model BASLER acA2040-25gc, 2048 × 2048 pixels) and a short lens (model Computar 2/3″ 8 mm f1.4). During the experiments, the temperature and light intensity of the laboratory, as well as the shutter speed and aperture of the camera, were kept constant. Images were processed using MATLAB to obtain the digital brightness I_d of three different regions of interest (Figure 1b) as explained in equation (6), and we calculated the mean value and standard deviation of all the images. We repeated this process with 21 different atomization rates ranging between 0 and 111 mg/s, which is the maximum achievable rate with this experimental setup (see Table S1 in the supporting information). A plot of digital brightness I_d versus normalized atomization rate $Q^* = m_v^*$ (Figure 1c) shows very good linear correlations in the three regions of interest (with correlation coefficients $R^2 \geq 0.98$). However, the slope and the ordinate in the origin of the best fit lines increase with the observation height of the image. As we show below, this is due to different incident radiation with height.

3.2. Influence of the Incident Radiation

The mass of saturated vapor m^s_{vap}, the number of droplets N, and thus the total mass of water m_v crossing the three regions of interest in Figure 1b (blue, red, and green sections) should be the same for a given atomization rate. Hence, if our model is correct, the different slope and ordinate in the origin we have found in Figure 1c must be explained by a changing incident radiation on the plume with height (as a consequence of a source of radiation at the ceiling of the laboratory). To confirm this, we write the digital brightness measured in the three sections as follows:

$$I_{d,\text{blue}} = a_{\text{blue}}\, m_v + b_{\text{blue}} \tag{7}$$

$$I_{d,\text{red}} = a_{\text{red}}\, m_v + b_{\text{red}} \tag{8}$$

$$I_{d,\text{green}} = a_{\text{green}}\, m_v + b_{\text{green}} \tag{9}$$

where the subscripts blue, red, and green refer to each one of the sections shown in Figure 1b. Note that here we do not account for the temporal variation of any parameter because the light intensity of the laboratory was constant. If we define $\Delta a_{x-\text{blue}} = a_x - a_{\text{blue}}$ and $\Delta b_{x-\text{blue}} = b_x - b_{\text{blue}}$, where x refers to red or green sections, we can write equations (8) and (9) as:

$$I_{d,x} = I_{d,\text{blue}} + \left[\Delta a_{x-\text{blue}} m_v + \Delta b_{x-\text{blue}}\right] \tag{10}$$

And rearranging the terms, we get:

$$I^c_{d,x} = I_{d,x} - \left[\Delta a_{x-\text{blue}} m_v + \Delta b_{x-\text{blue}}\right] = I_{d,\text{blue}} \tag{11}$$

where $I^c_{d,x}$ is the corrected digital brightness of the red and green sections. This equation means that if our model is consistent, the corrected digital brightness of the red and green sections should equal the digital brightness of the blue section. In the following, we express $\Delta a_{x-\text{blue}}$ and $\Delta b_{x-\text{blue}}$ in terms of parameters that can be determined from the images.

If we consider that the mixing ratio r and the specific humidity q are the same at the three analyzed regions, we obtain from the definition of a that $\Delta a_{x-\text{blue}}$ can be simply written as:

$$\Delta a_{x-\text{blue}} = \frac{\alpha[1 + rq]}{\hat{m}_d} \Delta f_{x-\text{blue}} \tag{12}$$

where $\Delta f_{x-\text{blue}} = f_x - f_{\text{blue}}$. On the other hand, if we consider that the mass of saturated vapor within the plume is the same in the three sections, we get from the definition of b that:

$$\Delta b_{x-\text{blue}} = \alpha \Delta I_{x-\text{blue}} - \frac{\alpha m^s_{\text{vap}}}{\hat{m}_d} \Delta f_{x-\text{blue}} \tag{13}$$

where $\Delta I_{x-\text{blue}} = I_x - I_{\text{blue}}$. By combining equations (11)–(13), considering again mass conservation, and taking into account that the number of droplets that crosses the three regions is the same, we finally obtain:

$$I^c_{d,x} = I_{d,x} - \Delta I^{c,1}_{d,\ x-\text{blue}} - \Delta I^{c,2}_{d,x-\text{blue}} \tag{14}$$

where $\Delta I^{c,1}_{d,\ x-\text{blue}} = \alpha N \Delta f_{x-\text{blue}}$ and $\Delta I^{c,2}_{d,x-\text{blue}} = \alpha \Delta I_{x-\text{blue}}$ are the corrector terms that can be calculated from the digital images. The term $\Delta I^{c,1}_{d,\ x-\text{blue}}$ can be interpreted from equation (2) as the difference of the brightness emitted from the droplets crossing the red and green sections and the droplets crossing the blue section. To determine this term, we first calculate the digital brightness of section *A′B′* (Figure 1b) in the three regions with equation (6) for all the atomization rates. Then, we subtract the digital brightness obtained in the same section *A′B′* when the atomization rate is zero. In such a way, the background intensity is removed. Finally, we subtract the results obtained for the blue region in the previous steps to the results obtained for the red and green regions. The second corrector term $\Delta I^{c,2}_{d,x-\text{blue}}$ is the digital brightness difference between the background of the red and green sections and the background of the blue section. To determine this term, we first calculate the digital brightness of section *AB* in the three regions with equation (6) when the atomization rate is zero, and then we subtract the result obtained for the blue section to the results obtained for the red and green sections. Once these correction terms are applied to $I_{d,\text{red}}$ and $I_{d,\text{green}}$ (equation (14)), we find that the digital brightness of the three regions versus the normalized atomization rate lies on the same straight line (Figure 1d). This result shows the consistency of the model.

3.3. Applicability of Our Experimental Results to Volcanic Plumes

Our experiments confirm a linear correlation between the water ejected by the ultrasonic humidifier and the digital brightness of the condensed plume. This implies that the absorption of the background light intensity by the droplets, and the multiple scattering within the cloud, can be neglected. This result can be directly extrapolated to actual volcanic clouds if the fraction of light blocked by the natural volcanic plumes (both the light coming from the background and the light scattered by the droplets) is lower than in the experimental plume. We check this condition by comparing the maximum column droplet density (i.e., the maximum number of droplets per unit area), which is given by *CD*, where *C* is the concentration of droplets in the part of the plume where the brightness is measured (number of droplets *N* per cubic meter of plume) and *D* is the plume diameter. Note that *CD* is the optical depth per cross section of a water droplet, whose value in our experiments and in volcanic clouds is similar (see section 3.1). The concentration *C* can be determined by writing equation (3) as follows:

$$C = \frac{[1 + rq]C_v - C^s_{\text{vap}}}{\hat{m}_d} \tag{15}$$

where C_v is the concentration of the water ejected by the humidifier or the volcano (mass of water m_v per cubic meter of plume) and C^s_{vap} is the concentration of saturated water vapor in the condensed plume (mass of saturated water m^s_{vap} per cubic meter of plume). The term $\hat{m}_d$ can be estimated from $\hat{m}_d \approx (4/3)\pi r_d^3 \rho_l$, where r_d is the radius of an average size water droplet and ρ_l is the density of liquid water. The terms C_v and C^s_{vap} can be estimated from $C_v = Q/Sv$ and $C^s_{\text{vap}} = q^s_{\text{vap}}\rho$, where Q is the water flux released by the humidifier or the volcano, S and v are the section and velocity of the condensed plume, respectively, q^s_{vap} is the specific humidity of the plume (mass of saturated water vapor per unit mass of gas mixture), and ρ is the partial density of the gas mixture in the plume (mass of gas mixture per cubic meter of plume), which can be approximated to the gas density (mass of gas mixture per cubic meter of gas within the plume) if we neglect the volume of condensed water versus the volume of gas. In turn, the specific humidity q and q^s_{vap} can be written as [e.g., *Fleagle and Businger*, 1980]:

$$q = \frac{\varepsilon\, e_S(T_{\text{air}})\ \text{RH}}{p - e_S(T_{\text{air}})(1 - \varepsilon)\text{RH}} \tag{16}$$

$$q^s_{\text{vap}} = \frac{\varepsilon\, e_S(T_p)}{p - e_S(T_p)(1 - \varepsilon)} \tag{17}$$

where $\varepsilon = M_w/M_d \approx 0.622$, with M_d being the molecular mass of dry air (~28.97 g/mol) and M_w being the molecular mass of water (~18.02 g/mol). Note that here we neglect the content of other much less abundant gases in the volcanic plume like SO_2 and CO_2. The terms $e_S(T_{\text{air}})$ and $e_S(T_p)$ are the saturation vapor pressure at the temperature of the air T_{air} and at the temperature of the plume T_p, respectively; RH is the relative humidity of the air; and p is the pressure at crater levels. The saturation vapor pressure can be estimated for a given temperature T from the corrected Clausius-Clapeyron equation [*Koutsoyiannis*, 2012]:

$$e_S(T) = A_1 e^{A_2(T - A_3)/T}\left(\frac{A_3}{T}\right)^{A_4} \tag{18}$$

where $A_1 = 611.657$, $A_2 = 24.921$, $A_3 = 273.16$, and $A_4 = 5.06$. With these values of the constants, both the temperature T and the saturation pressure $e_S(T)$ are in SI units. Finally, the mean plume temperature T_p is related to the mixing ratio and air temperature through [e.g., *Matsushima and Shinohara*, 2006]:

$$T_p = \frac{C_w T_w + rC_{\text{air}}T_{\text{air}}}{C_w + rC_{\text{air}}} \tag{19}$$

where C_w and T_w are the specific heat capacity of water vapor and the volcanic gas temperature, respectively, and C_{air} and T_{air} are the specific heat capacity and temperature of the air, respectively. From now on, we consider that $C_w \approx 2.0$ kJ/kg K and $C_{\text{air}} \approx 1.0$ kJ/kg K [e.g., *Fleagle and Businger*, 1980]. By combining equations (15)–(19), we can estimate the concentration of droplets both in our experiments and in volcanic plumes.

In our experiments, the maximum flux reached was $Q \approx 111$ mg/s, the section of the plume is given by the diameter of the nozzle from which the droplets exit the humidifier ($D = 15$ mm), and the velocity is on the order of $v \sim 5$ cm/s (estimated by comparing images). For $T_w \sim T_{\text{air}} \sim 20$°C (ultrasonic humidifiers create

Table 1. Estimation of the Column Droplet Density in Condensed Volcanic Plumes

Parameters and Units	Value	Range[a]						
Gas temperature T_w (°C)	1000	700–1300	---	---	---	---	---	---
Air temperature T_{air} (°C)	15	---	5–25	---	---	---	---	---
Mixing ratio r[b]	500	---	---	50–5000	---	---	---	---
Relative humidity RH (%)	30	---	---	---	10–90	---	---	---
Steam flux Q (kg/s)	50	---	---	---	---	20–200	---	---
Plume diameter D (m)	20	---	---	---	---	---	5–40	---
Plume velocity v (m/s)	2	---	---	---	---	---	---	0.5–5
Plume temperature T_p(°C)[c]	18.9	17.7–20.1	9.0–28.9	15.4–52.9	---	---	---	---
Gas density ρ (kg/m^3)[d]	0.75	~0.75	0.73–0.78	0.67–0.76	---	---	---	---
Droplet concentration $C(\cdot 10^6$drops/cm$^3)$	0.37	~0.37	0.26–0.56	0.06–2.53	0.21–0.85	0.14–1.55	0.08–6.24	0.14–1.55
Column droplet density $CD(\cdot 10^9$drops/cm$^2)$	0.74	0.74–0.75	0.53–1.13	0.11–5.06	0.42–1.71	0.27–3.09	0.31–3.12	0.27–3.09

[a] The parameters with the dashed line are not varied, and their values are given in the second column.

[b] The mixing ratio is varied between $r = 50$ and $r = 5000$ to obtain plume temperatures close to the air temperature or up to some tens of degrees [*Witter et al.*, 2012; *Conde et al.*, 2014].

[c] The temperature of the plume is calculated with equation (19).

[d] The gas density is calculated by assuming and ideal gas approach from the temperature of the plume T_p and atmospheric pressure $p \sim 1$ atm. As in the experimental plume, we consider $r_d \sim 5$ µm [*Gassó*, 2008] and $\rho_l \sim 1000$ kg/m^3.

cool fog, so we consider room temperature), $p \sim 1$ atm, $r_d \sim 5$ µm, $\rho_l \sim 1000$ kg/m^3, RH ~ $60 - 70\,\%$, $r \sim 50 - 5000$, and calculating ρ from an ideal gas approach, we obtain that the maximum droplet concentration of our experiments is on the order of $C \sim 10^7 - 10^9$ drops/cm^3. Hence, the column droplet density in our experiments reaches values in the range of $CD \sim 10^7 - 10^9$ drops/cm^2. The same calculations are done for volcanic plumes, and we obtain that the column droplet density reaches values in the range $CD \sim 10^8 - 10^9$ drops/cm^2 for many scenarios (Table 1). For example, for volcanic gas temperatures of $T_w \sim 1000$°C, atmospheric temperature $T_{\text{air}} \sim 15$°C, mixing ratio $r \sim 500$, relative humidity RH ~ 30 %, steam flux $Q = 50$ kg/s, ascent velocities $v \sim 2$ m/s, and plume diameters $D \sim 20$ m, we obtain that the column droplet density is $CD \sim 7.4 \cdot 10^8$ drops/cm^2. Therefore, we conclude that at least in diluted volcanic plumes, the column droplet density is at most on the same order of magnitude than the column droplet density we have reached in our experiments. Thus, we can assure the linear correlation between the brightness of condensed volcanic clouds and its volcanogenic water content in a wide range of scenarios. More experiments are required to determine the maximum column droplet density (or optical depth) from which the linear correlation is not fulfilled anymore.

4. Processing Method of the Brightness Time Series of a Volcanic Plume

The variability of the terms $a(t)$ and $b(t)$ in equation (5) must be corrected in a brightness time series to ensure that a brightness change is only due to a vapor emission change. As we stated above, we use $a(t) = \alpha f(t)[1 + r(t)q(t)]/\hat{m}_d$ and $b(t) = \alpha\left[I_b(t) - m^s_{\text{vap}}(t)f(t)/\hat{m}_d\right]$. The term $f(t)$ accounts for the scattering of each water droplet and varies gradually during the day with the incident solar radiation on the plume, the angle Sun-plume-observer, and the mean water droplet size [e.g., *Lock and Yang*, 1991; *Han et al.*, 1994; *Zuidema and Harunann*, 1995; *Gassó*, 2008; *Hergert and Wriedt*, 2012]. The term $I_b(t)$ accounts for the background radiation of the region of interest that is analyzed and thus also varies with the position of the Sun during the day. The variability of the mass of saturated water vapor $m^s_{\text{vap}}(t)$ depends on the temperature and pressure, and thus depends indirectly on the temperature of the volcanic gas, temperature, pressure, and relative humidity of the atmosphere, and mixing ratio between air and volcanic gases [e.g., *McGonigle et al.*, 2004; *Matsushima*, 2005; *Matsushima and Shinohara*, 2006]. The volcanic gas temperature depends on magma temperature, and thus, we consider it constant during quiescence, at least over short time scales of hours or days; temperature, pressure, and relative humidity of the atmosphere (and hence specific humidity $q(t)$ as well—see equation (16)) fluctuate on a diurnal time scale [e.g., *McGonigle et al.*, 2004]; and the mixing ratio $r(t)$ depends on the entrainment of air into the plume, which can be considered constant with time as long as a buoyant quiescent plume is geometrically stable, that is, as long as there are no important changes of wind speed and direction at crater heights [e.g., *Bursik*, 2001; *Suzuki and Koyaguchi*, 2010]. Therefore, at least for stable buoyant plumes, the terms $a(t)$ and $b(t)$ are expected to show long-term trends that in principle can be corrected. Short-term irregular variations of $a(t)$ and $b(t)$ can also occur if an atmospheric cloud, or a part of the downstream gas plume, interposes between the Sun and the section of plume that is analyzed. In the following, we describe a strategy to correct long-term trends and irregular perturbations in a brightness time series:

1. *Choice of regions of interest*. We calculate the digital brightness according to equation (6) in three regions of the images: (R1) in a section of the plume, which accounts for the temporal variation of the background, incident light, weather conditions at crater level, and steam emissions; (R2) outside the plume but with the same background, which accounts for the temporal variation of the background; and (R3) in the crater rim right below the section of the plume, which accounts for irregular and gradual temporal variations of the incident solar light on the crater.
2. *Light change correction*. We divide the brightness values at (R1), (R2), and (R3) by the number of pixels of each region and remove the mean of the resulting time series. Then, we subtract the mean-removed time series of regions (R2) and (R3) to the mean-removed time series of (R1). By doing this, we are removing irregular and gradual trends induced by the changing incident light, the trend induced by the changing background, and even possible perturbations induced by instabilities of the digital camera. With this approach, we use brightness changes of (R3) as a proxy for the changes of the incident solar light on (R1), which is realistic if both regions are spatially very close and as long as the Sun is not on the opposite side of the volcano from the position of the camera.
3. *Weather change correction*. Whatever trend remains in the brightness time series of the region (R1) should be only the consequence of changes in the atmospheric conditions at crater levels. By assuming that these changes are long term (with diurnal or semidiurnal periodicity), detrending can be done by fitting a low-order polynomial to the time series and then subtracting the best fit to the brightness data. This undesirable long-term trend could be also removed by filtering the data with a high-pass filter.

For simplicity, we suggest standardizing (i.e., normalizing) the resulting time series of the region (R1) by subtracting the mean value of the time series to each datum and dividing by the standard deviation. This is not a requirement, but it produces a dimensionless time series which allows a direct comparison with the normalized time series of other volcanic gases like SO_2 (as we show in the next section). Normalization does not alter the spectral content of the signal.

5. Case Studies

Below, we determine the spectral features of the steam emissions from two volcanoes. First, we analyze the steam pulses from Mount Erebus by computing the digital brightness from a movie of the gas plume recorded on 26 December 2006 by *Boichu et al*. [2010]. This brightness time series is compared with an SO_2 time series that was measured during the same period. Second, we analyze the steam cycles of Mount Mayon by computing the digital brightness time series corresponding to a set of digital images we took on 4 March 2014.

5.1. Erebus Volcano

Mount Erebus is a basaltic stratovolcano located in Ross Island, Antarctica, which is known for its convective lava lake persisting since 1972. Lava lake activity, characterized by passive gas emissions with average SO_2 flux on the order of 60 t/d, is interspersed by more or less frequent minor explosions and by larger Strombolian paroxysms occurring occasionally [e.g., *Calkins et al*., 2008; *Davies et al*., 2008; *Johnson et al*., 2008; *Sweeney et al*., 2008].

Digital images of the condensed gas plume were extracted from a 30 min movie that was recorded on 26 December 2006 (movie supplied by M. Boichu, personal communication and partially published in *Boichu et al*. [2010]). The movie was split into frames, and one frame per second of shooting was analyzed (sampling frequency of 1 Hz). With these frames, we calculated the digital brightness of a region of interest (R1) that crosses the volcanic plume above the crater rim (red section of Figure 2a), which in turn coincides with the section where *Boichu et al*. [2010] measured the SO_2 column amounts (molecules of SO_2/cm^2). To apply the correction strategy explained in the previous section, we also calculated the brightness time series in two auxiliary regions (R2) and (R3): region (R2) is centered in the sky close to the

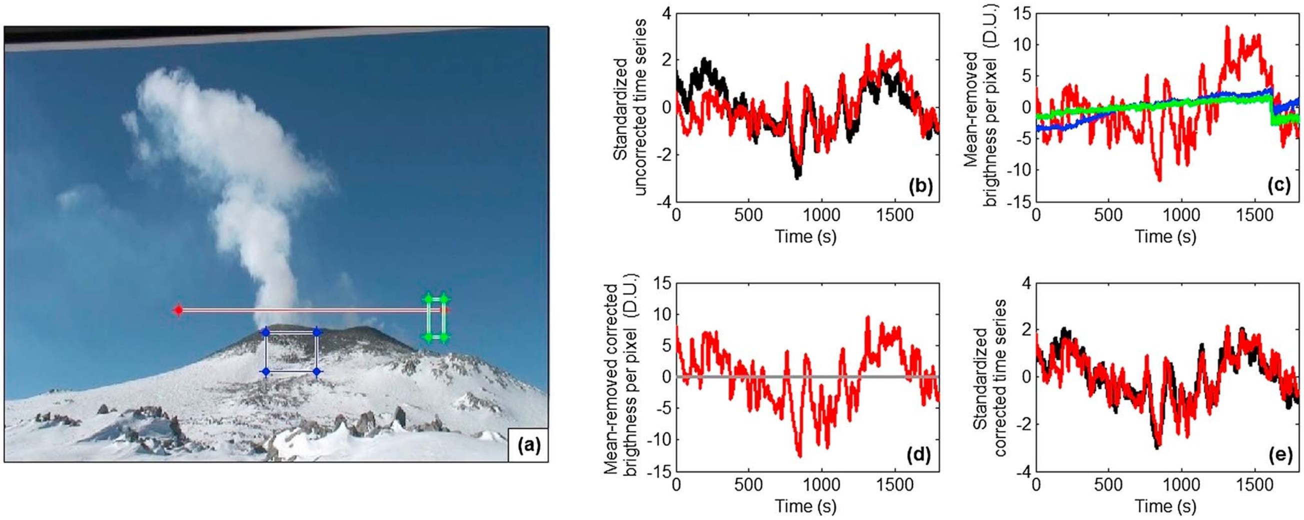

Figure 2. Digital brightness analysis of the plume of Erebus volcano and comparison with SO_2 time series. (a) Image of the movie recorded at Erebus volcano on 26 December 2006 (movie partially published by *Boichu et al*. [2010]; complete movie by courtesy of M. Boichu, personal communication). The red line is the region (R1) of interest where we perform the analysis. The green and blue regions are the (R2) and (R3) auxiliary regions, respectively, that we use to correct the brightness time series. (b) Standardized SO_2 (black) and raw brightness (red) time series. (c) Mean-removed digital brightness in digital units (DUs) of the (R1), (R2), and (R3) regions. (d) Mean-removed digital brightness of the region (R1) after the light change correction. The gray line is the first-order polynomial that best fit to the brightness curve and which is used for the weather change correction (slope = −1.6e-5 and ordinate in the origin = 0.01). (e) Comparison between standardized SO_2 time series (black) and standardized and corrected brightness time series (red).

plume, and region (R3) is centered in the upper left part of the crater rim (green and blue polygons of Figure 2a, respectively).

Local peaks and troughs of the brightness time series of the region (R1) are in general well correlated with those corresponding to the SO_2 time series (e.g., time window 500–1000 s in Figure 2b). However, there is also an increasing trend of the brightness with time that is not present in the SO_2 data and that is not likely due to a gradual increase of the water emissions because it is also observed in the regions (R2) and (R3) of the image (Figure 2c). A sudden brightness drop is also observed in (R2) and (R3) at t ~ 1620 s, which could be due to a fault in the power supply of the camera. These gradual and irregular changes of the brightness time series are removed from (R1) as explained in the light change correction step of the previous section, and then a first-order polynomial is fitted to the resulting time series to make the weather change correction (Figure 2d). The slope of the fitting straight line is very low, thus suggesting that atmospheric parameters like temperature and relative humidity remained almost invariant during the 30 min shooting that we analyzed. The standardized and corrected digital brightness time series, and the standardized SO_2 column amounts time series, are now very similar (Figure 2e).

The wavelet transform analysis of the time series shows that there are not steady periodic pulses in the whole time series and reflects that steam emissions actually emerge from a mix of finite pulses with different periodicities. In particular, we identified two main periodic bands (Figure 3a). Band 1 contains the more energetic component, which appears between 500 and 1400 s of the time series with periodicities in the range of ~100–250 s. Band 2 is less energetic, and the periodicity is in the range of ~500–650 s. Some short-duration periodic components with periodicities lower than 100 s also appear irregularly through the time series. The fast Fourier transform shows that digital brightness, and thus steam emissions, follows a well-defined fractal (power law) distribution in a wide range of frequencies of the spectrum. That is, $\Delta \sim \nu^{\gamma}$, where Δ is the amplitude of the pulse, ν is the frequency, and γ is a constant which in this case is $\gamma \approx -1$ (Figure 3b).

The wavelet transform of the SO_2 signal also shows the bands 1 (~100–250 s) and 2 (~500–650 s), but there is a third band appearing at least between 500 and 1300 s with periodicities in the range of ~300–450 s (Figure 3c). The fractal distribution is not so evident for the SO_2 time series because there is a clear deviation from a power law distribution for periodicities lower than ~12 s (Figure 3d), even though the best fit for larger

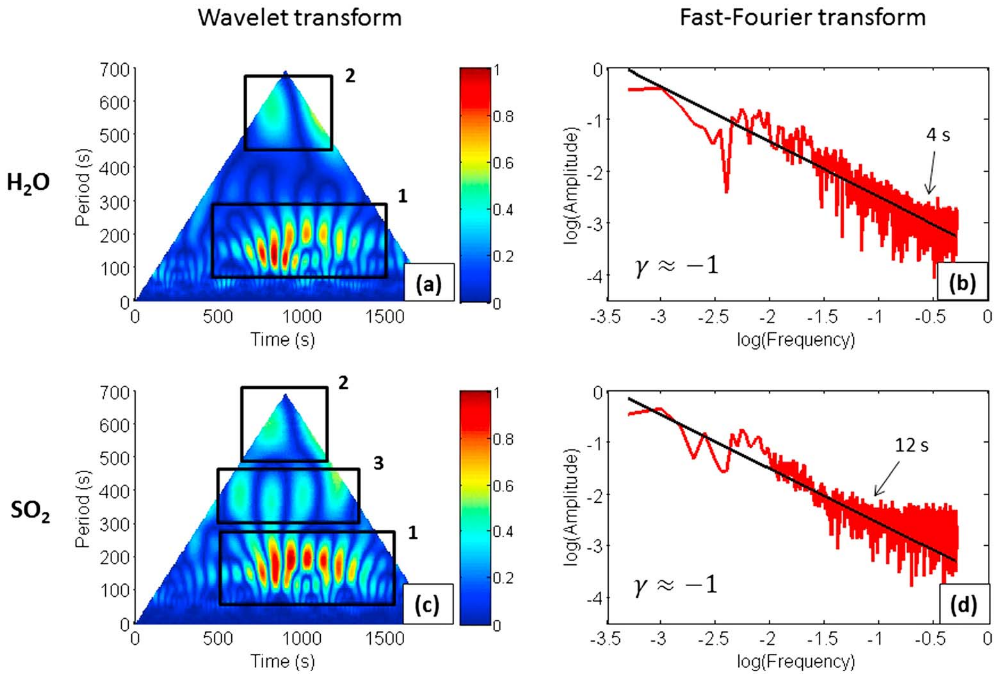

Figure 3. Spectral features of the H_2O and SO_2 emissions from Erebus volcano. (a) Wavelet transform of the brightness time series. The colors represent the normalized amplitude, and the rectangles indicate the more characteristic periodic components of the time series. (b) Fast Fourier transform of the brightness time series (red) and best fit line (black). (c) Wavelet transform of the SO_2 time series (data from *Boichu et al.* [2010]). (d) Fast Fourier transform of the SO_2 time series (red) and best fit line for periodicities larger than 12 s (black). Wavelet (Morlet algorithm) and fast Fourier transforms are calculated by using MATLAB. In Figures 3a and 3c, the cone of influence (part of the spectrum that is affected by edge effects) is removed. In Figures 3b and 3d, γ is the slope of the best fit line.

periodicities also gives an exponent of $\gamma \approx -1$. Power law deviation at high frequencies is also observed in the fast Fourier transform of the brightness time series but only for periodicities lower than ~4 s (compare Figures 3b and 3d).

5.2. Mayon Volcano

Mayon is a basaltic-andesitic stratovolcano located to the north of Legazpi City, more than 300 km southeast of Manila, the capital city of the Philippines. This volcano is known by its almost perfect conical shape that extends from the sea level up to almost 2500 m height, and its activity is characterized by persistent passive degassing (with average SO_2 fluxes around 100–500 t/d, according to the reports published online in http://www.phivolcs.dost.gov.ph by the Philippine Institute of Volcanology and Seismology). Passive degassing is interspersed by mildly explosive eruptions occurring every few years, and large explosive eruptions occur every 100 years or so [e.g., *Siebert et al.*, 2010].

Digital images of Mayon crater and plume were taken with an IP camera (model BASLER acA2040-25gc, 2048 × 2048 pixels, with lens Tamron A08N SP AF200–500 mm F/5–6.3) located at the volcano observatory, which is about 12 km southeast of the crater. One image per second was taken continuously during 106 min from 6:50 A.M. to 8:36 A.M. on 4 March 2014, period during which the plume rose vertically. We chose a region (R1) right in the crater rocks (red section of Figure 4a) and an auxiliary region right below the crater (blue polygon of Figure 4a). The choice of (R1) right in the crater rocks is advantageous because the perturbation of the plume by wind changes is minimized, and the auxiliary region represents both (R2) and (R3) since the crater rocks are the background of (R1) in this case.

The standardized raw brightness data show an increasing trend of the brightness with time (Figure 4b). This is also observed in the auxiliary region of the image (Figure 4c), thus suggesting that is not related to a long-term increase of the water vapor emissions. Irregular brightness changes are also observed in (R2) (=(R3)), maybe because of stability problems of the camera. The trend of (R2) (=(R3)) is removed twice to

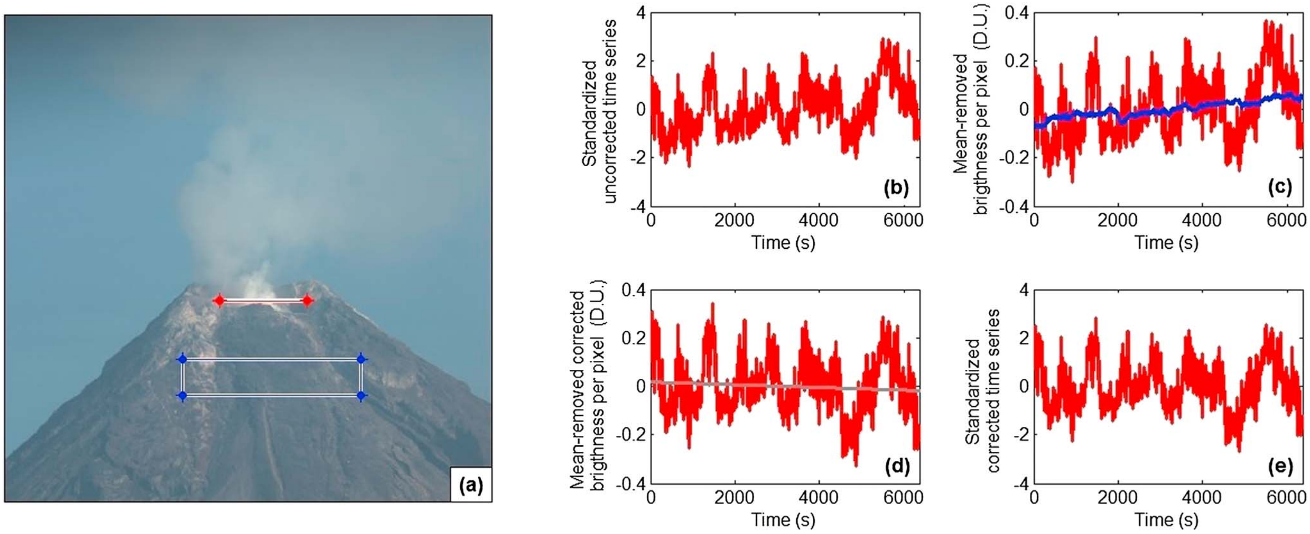

Figure 4. Digital brightness analysis of the plume of Mayon volcano. (a) Summit of Mayon volcano as viewed from the observation point. The red line is the region (R1) of interest where we perform the analysis. The blue region (R2) (=(R3)) is the auxiliary region we use to correct the brightness time series for light and weather change. (b) Standardized raw brightness time series. (c) Mean-removed digital brightness in digital units (DUs) of the (R1) and (R2) (=(R3)) regions. (d) Mean-removed digital brightness of the region (R1) after the light change correction. The gray line is the first-order polynomial that best fits to the brightness curve and which is used for the weather change correction (slope = −5.6e-6 and ordinate in the origin = 0.02). (e) Standardized and corrected brightness time series.

the time series of (R1), and then a first-order polynomial is fitted to the resulting data to make the weather change correction (Figure 4d). The slope of the fit is slightly negative, suggesting a possible slight increase of temperature and decrease of relative humidity during the studied period, which is realistic during dawn [e.g., *McGonigle et al.*, 2004]. The standardized and corrected digital brightness time series shows a quite regular behavior of the steam emissions (Figure 4e).

The wavelet transform of the brightness signal shows four characteristic bands (Figure 5a). Band 1, in the range of ~100–500 s, contains short-duration periodic components appearing intermittently. Band 2 contains a quite stable periodic component (~1 h) in the range of ~600–900 s, even though the amplitude gradually decreases with time. Band 3 also contains a very stable periodic signal in the range of ~1200–1600 s, and contrary to band 2, the amplitude gradually increases with time. One more periodic band is observed around 2000 s, even though it is close to the limit detectable with the wavelet transform. Just as at Erebus, the wavelet transform shows that there is no steady pulse during the whole time series, since, although there are long-duration periodic components (~1 h), their amplitudes change gradually.

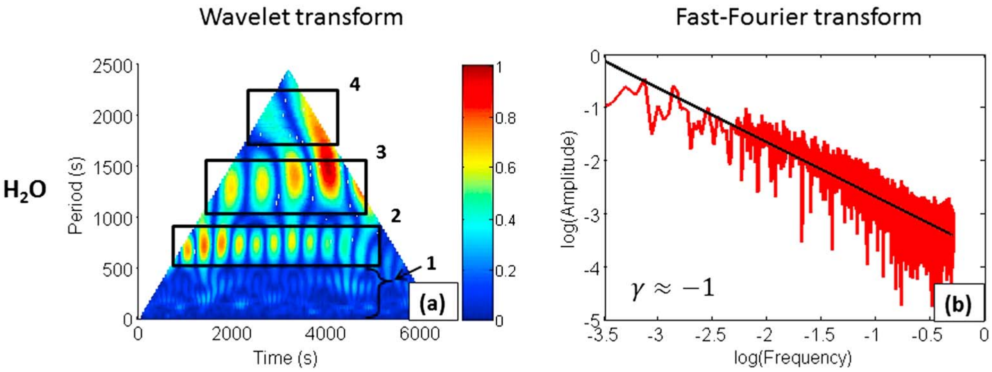

Figure 5. Spectral features of the H_2O emissions from Mayon volcano. (a) Wavelet transform of the brightness time series. The colors represent the normalized amplitude, and the rectangles indicate the more characteristic periodic components of the time series. The cone of influence (part of the spectrum that is affected by edge effects) is removed. (b) Fast Fourier transform of the brightness time series (red) and best fit line (black). The parameter γ is the slope of the best fit line. Wavelet (Morlet algorithm) and fast Fourier transform are calculated by using MATLAB.

The frequency spectrum of the brightness time series of Mayon also follows a well-defined fractal (power law) distribution with exponent $\gamma \approx -1$ (Figure 5b).

6. Discussion

6.1. Limitations and Uncertainties of the Brightness Method

The main limitation of our method is that it can be only applied when the volcanic plume saturates, a condition that, however, is very common at many active volcanoes under typical atmospheric conditions at crater heights [*Matsushima*, 2005; *Matsushima and Shinohara*, 2006]. Complications can arise from external perturbations that can contaminate the brightness time series with undesired trends. However, these trends can be corrected because they follow well-defined long-term cycles, such as the semidiurnal and diurnal variations of pressure, temperature, and humidity [e.g., *Zimmer and Erzinger*, 2003; *McGonigle et al.*, 2004], and the possible daily change of the water droplet size [e.g., *Han et al.*, 1994; *Zuidema and Harunann*, 1995]. Other long-term trends, like those caused by the changing incident radiation on the plume due to the changing position of the Sun along the day, can also be corrected by analyzing different auxiliary regions of the digital images. The same strategy can be used to correct short-term perturbations of brightness time series, like those caused by instabilities of the camera, or by clouds interposing between the Sun and the analyzed region of the plume.

Other processes, like wind changes at crater heights, could induce uncontrolled and fast variations of the mixing ratio between air and volcanic gas r [e.g., *Bursik*, 2001]. Short-term changes of the mixing ratio can modify the temperature of the condensed plume T_p, the concentration of droplets C with time, and thus the brightness measurements. For example, for the parameters in Table 1 (column 2), we obtain by using equation (19) that the temperature of the plume T_p varies around 6°C when the mixing ratio varies from $r = 250$ to $r = 1000$. This variation of the mixing ratio would induce a change of C in the range $(2.5 - 6.1) \cdot 10^5\ \mathrm{cm}^3$, whose mean value and absolute uncertainty is $(4.3 \pm 1.8) \cdot 10^5\ \mathrm{cm}^3$. This implies a relative uncertainty for the brightness measurements on the order of 40%, which is realistic for stable ascending plumes since the range of variation of T_p in short time scales is estimated on the order of a few degrees [e.g., *Witter et al.*, 2012; *Conde et al.*, 2014], like the variation of T_p that we have considered above. Uncertainty of 40% is on the same order of magnitude than the uncertainty typically assigned to the SO_2 concentrations and fluxes measured with absorption spectrometers [e.g., *Boichu et al.*, 2010].

Another factor that could increase the brightness uncertainty is the variation of the molar ratio $[H_2O]/[HCl]$ in the plume because the dissolution of HCl in water droplets affects the saturation vapor pressure and hence can modify the mass of saturated water and the number of water droplets itself [*Matsushima and Shinohara*, 2006]. This ratio has been found to remain roughly constant during quiescence at volcanoes like Masaya [*Burton et al.*, 2000], and thus, we do not take into account this possibility. In any case, short-term sporadic perturbations are not expected to obscure the overall spectral features of sufficiently long brightness time series [e.g., *Boichu et al.*, 2010].

6.2. Interpretation of the Degassing Patterns From Erebus and Mayon Volcanoes

In the following, we discuss the processes that could explain the overall results we have obtained from Erebus and Mayon volcanoes. That is, periodic gas emissions with finite duration, a periodic component in the band ~300–450 s that appears in the SO_2 time series of Erebus but that is absent in the brightness time series, and the fractal distribution of the frequency spectra.

6.2.1. Periodic Gas Emissions With Finite Duration

Several mechanisms could explain periodic patterns during quiescence. For example, pulsed entrance of magma into the lava lake could explain gas fluctuations at Erebus [*Oppenheimer et al.*, 2009]; the non-Newtonian rheology of magmas can lead spontaneously to the alternation between bubbly regime, with quasiperiodic release of gas, and channeling regime, in which bubbles percolate through the magma column [*Divoux et al.*, 2011]; and the presence of geometrical or rheological barriers in the magma plumbing system (e.g., reservoir roof [*Jaupart and Vergniolle*, 1988], cavities in the conduit [*Boichu et al.*, 2010], or viscoelastic layers formed beneath the magma level [*Patrick et al.*, 2011]) can lead to the cyclical formation and collapse of foams. Although these mechanisms could explain periodic gas emissions, a model able to reproduce completely the spectral features of volcanic degassing time series is still missing.

6.2.2. Difference Between the Brightness and SO_2 Wavelet Transforms of Erebus Volcano

The corrected brightness and SO_2 time series are in general very similar (Figure 2e), thus suggesting that the molar ratio $[H_2O]/[SO_2]$ during the passive degassing period analyzed varies very little. However, the spectral analysis reveals that the SO_2 time series contains a periodic component in the band 300–450 s (band 3) that is absent in the brightness time series. This component lasts for at least 700 s, which suggests that it is not the result of short-term effects like changes in the mixing ratio or vent gas temperature. Another possibility could be that water droplets do not follow the same path as the molecules of SO_2 during plume ascent, but it does not seem feasible in this frequency range because bands 1 and 2, with higher and lower periodicities than band 3, appear very clearly in both time series (Figure 3). Therefore, band 3 likely reflects a real volcanic process. We propose that band 3 might be only present in the SO_2 time series because it is induced by periodic trains of bubbles exsolved from very hot magma batches. In such a case, the thermochemical reaction $H_2S + H_2O \leftrightarrow SO_2 + 3H_2$ shifts to the right, thus favoring bubbles with higher concentrations of SO_2 and lower concentrations of H_2O [e.g., *Sigurdsson et al.*, 1999; *Oppenheimer and Kyle*, 2008]. On the other hand, bands 1 and 2 might be present in both time series because they are induced by periodic trains of bubbles exsolved from cooler magmas, such that the amount of H_2O is not reduced. This idea of magmas with different temperatures is consistent with magma convection in the conduit, as it has been proposed for Erebus in many studies [e.g., *Oppenheimer et al.*, 2009; *Molina et al.*, 2012].

6.2.3. Fractal Frequency Spectra

The fast Fourier transform analysis of the brightness time series of Erebus and Mayon volcanoes reveals that the larger the amplitude of the steam pulses, the lower the frequency. This feature likely reflects a volcanic process, instead of atmospheric, since turbulent eddies only affect very high frequencies (periodicities lower than ~40 s [*Tamburello et al.*, 2013]). For example, the frequency spectra could reflect the presence of geometrical or rheological barriers of different sizes because the larger the section of the barrier where bubbles accumulate, the larger the volume of the foam and the lower the collapsing frequency (as it can be inferred from the experiments performed by *Jaupart and Vergniolle* [1989]). However, the problem is likely much more complex because fractal (power law) frequency spectra emerge from the coupling between the different parts that compose a dynamic system which can be in a self-organized critical state [e.g., *Bak et al.*, 1987; *Bak*, 1996; *Turcotte*, 1999]. Hence, we propose that Erebus and Mayon volcanoes are self-organized critical systems, such that degassing patterns arise spontaneously from the coupling between bubble ascent through the conduit [*Vergniolle and Jaupart*, 1986], intermittent bubble bursting [*Yano et al.*, 2004; *Kaulakys et al.*, 2005], magma convection in the conduit [e.g., *Shinohara*, 2008], or changes of conduit permeability [*Michaut et al.*, 2009; *Divoux et al.*, 2011]. Experimental and numerical research is required to understand the conditions that determine the exponent of the power law and to unveil how it varies during an unrest episode. Self-organized critical behavior was already proposed for the gas pistoning activity of Kilauea volcano after the analysis of seismic tremor signals [*Chouet and Shaw*, 1991].

Contrary to the frequency spectrum of the brightness time series of both volcanoes, which shows well-defined power law distributions along a wide range of frequencies, the spectrum of the SO_2 time series of Erebus clearly deviates from a power law for periodicities lower than ~12 s. We propose that this can be consequence of an external perturbation. The gas molecules, which is what is monitored with absorption spectrometers or UV cameras, have a mass many orders of magnitude lower than the mass of a micrometric water droplet, which is what we monitor with the brightness method (the weight of a molecule of SO_2 is on the order of 10^{-25} kg, whereas the weight of micrometric water droplets is on the order of 10^{-13} kg). Because of this much lower mass, the inertia of the SO_2 molecules during plume ascent is much lower than the inertia of the water droplets, and thus, it is feasible that the local wind of the crater area perturbs more the motion of the molecules than the motion of the droplets. This is patent for high frequencies (low periodicities) because they are less energetic. Alternatively, the deviation from a power law behavior could also be consequence of a sensor-dependent process.

7. Conclusions

We have reported a new method to capture remotely the spectral features of the H_2O volcanic emissions, which is by far the major component of most volcanic plumes. This can be done simply by analyzing digital images since there is a correlation between the brightness of condensed volcanic clouds and its volcanogenic water content. Our method is based on the light scattered by the micrometric droplets moving with the plume, and it allows real-time monitoring of the steam cycles with low maintenance, is low cost since only requires a commercial digital camera to measure brightness changes and a laptop for data processing, the sampling rate can be very large (limited by the specs of the digital camera), data processing is relatively straightforward, can be used far away from the volcanic vent with proper amplification lens (making it especially useful for hardly accessible volcanoes), and external disturbances caused by wind changes are minimized since brightness can be measured right in the crater area. Hence, digital brightness analysis can become an ideal method for real-time monitoring of steam cycles at many active volcanoes.

Our research also opens the possibility of developing more complex systems able to measure the absolute values of the steam flux. This could be done by combining luminance measurements with real-time tracking of the position of the Sun along the day and with simultaneous measurements of the atmospheric parameters at crater levels (relative humidity, pressure, and temperature). Alternatively, absolute values of the steam flux could also be monitored in real-time after a previous calibration of the brightness values. This calibration can be performed by combining digital images with simultaneous measurements of SO_2 gas fluxes (derived with ultraviolet absorption spectrometers or UV cameras) and $[H_2O]/[SO_2]$ ratios (derived with OP-FTIR).

We have applied the brightness method to two digital movies from Erebus and Mayon volcanoes. And we have found that H_2O degassing time series contain finite but well-defined periodic components and that some periodic components appear both in H_2O and SO_2 time series, but others do not. In addition, the frequency spectra of the brightness time series of both volcanoes reveal that the steam emissions exhibit very well defined fractal behavior in a wide range of frequencies. These findings suggest that quiescent degassing cannot be understood from a unique steady periodic mechanism but that it emerges as a self-organized critical phenomenon from the complex coupling of different processes.

Acknowledgments
Contact the corresponding author to download the images used for the brightness analysis in the experiments and in the case studies. We thank the comments and suggestions of A. Aiuppa, an anonymous reviewer, and the Associate Editor, which helped to improve the manuscript. We also thank M. Manga, C. Bouvet de Maisonneuve, P. Allard, and C. Newhall for their comments on the subjects of this manuscript and M. Boichu for sharing her movies of the plume of Erebus volcano. The technical support given by A. Schmidt, M. Bornas, and A. Baloloy is gratefully acknowledged. This work comprises Earth Observatory of Singapore contribution 90. This research is supported by the National Research Foundation Singapore and the Singapore Ministry of Education under the Research Centres of Excellence initiative.

References

Aiuppa, A., G. Giudice, S. Gurrieri, M. Liuzzo, M. Burton, T. Caltabiano, A. J. S. McGonigle, G. Salerno, H. Shinohara, and M. Valenza (2008), Total volatile flux from Mount Etna, *Geophys. Res. Lett.*, *35*, L24302, doi:10.1029/2008GL035871.

Allard, P., M. Burton, and F. Mure (2005), Spectroscopic evidence for a lava fountain driven by previously accumulated magmatic gas, *Nature*, *433*, 407–410, doi:10.1038/nature03246.

Bak, P. (1996), *How Nature Works: The Science of Self-Organized Criticality*, Copernicus, New York.

Bak, P., C. Tang, and K. Wiesenfeld (1987), Self-organized criticality: An explanation of 1/f noise, *Phys. Rev. Lett.*, *59*, 381–384, doi:10.1103/PhysRevLett.59.381.

Bala, R., and K. Braun (2004), Color-to-grayscale conversion to maintain discriminability, *Proc. SPIE*, *5293*, 196–202.

Bohren, C. F., and D. R. Huffman (2004), *Absorption and Scattering of Light by Small Particles*, 1st ed., Wiley-VCH, Weinheim, Germany.

Boichu, M., C. Oppenheimer, V. Tsanev, and P. R. Kyle (2010), High temporal resolution SO_2 flux measurements at Erebus volcano, Antarctica, *J. Volcanol. Geotherm. Res.*, *190*, 325–336, doi:10.1016/j.jvolgeores.2009.11.020.

Branan, Y. K., A. Harris, I. M. Watson, J. C. Phillips, K. Horton, G. Williams-Jones, and H. Garbeil (2008), Investigation of at-vent dynamics and dilution using thermal infrared radiometers at Masaya volcano, Nicaragua, *J. Volcanol. Geotherm. Res.*, *169*, 34–47, doi:10.1016/j.jvolgeores.2007.07.021.

Bursik, M. (2001), Effect of wind on the rise height of volcanic plumes, *Geophys. Res. Lett.*, *28*, 3621–3624, doi:10.1029/2001GL013393.

Burton, M., C. Oppenheimer, L. A. Horrocks, and P. W. Francis (2000), Remote sensing of CO_2 and H_2O emission rates from Masaya volcano, Nicaragua, *Geology*, *28*, 915–918, doi:10.1130/0091-7613(2000)28<915:RSOCAH>2.0.CO;2.

Calkins, J., C. Oppenheimer, and P. R. Kyle (2008), Ground-based thermal imaging of the lava lakes at Erebus volcano, Antarctica, *J. Volcanol. Geotherm. Res.*, *177*, 695–704, doi:10.1016/j.jvolgeores.2008.02.002.

Chouet, B., and H. R. Shaw (1991), Fractal properties of tremor and gas piston events observed at Kilauea volcano, Hawaii, *J. Geophys. Res.*, *96*, 10,177–10,189, doi:10.1029/91JB00772.

Conde, V., P. Robidoux, G. Avard, B. Galle, A. Aiuppa, A. Muñoz, and G. Giudice (2014), Measurements of volcanic SO_2 and CO_2 fluxes by combined DOAS, Multi-GAS and FTIR observations: A case study from Turrialba and Telica volcanoes, *Int. J. Earth Sci.*, *103*, 2335–2347, doi:10.1007/s00531-014-1040-7.

Davies, A. G., J. Calkins, L. Scharenbroich, R. G. Vaughan, R. Wright, P. Kyle, R. Castaño, S. Chien, and D. Tran (2008), Multi-instrument remote and in situ observations of the Erebus volcano (Antarctica) lava lake in 2005: A comparison with the Pele lava lake on the Jovian moon Io, *J. Volcanol. Geotherm. Res.*, *177*, 705–724, doi:10.1016/j.jvolgeores.2008.02.010.

Divoux, T., V. Vidal, M. Ripepe, and J. C. Géminard (2011), Influence of non-Newtonian rheology on magma degassing, *Geophys. Res. Lett.*, *38*, L12301, doi:10.1029/2011GL047789.

Findeisen, J., M. Gnirß, N. Damaschke, H. P. Schiffer, and C. Tropea (2005), 2D-concentration measurements based on Mie scattering using a commercial PIV system, paper presented at 6th Int. Symp. on Particle Image Velocimetry, Pasadena, California.

Fleagle, R. G., and J. A. Businger (1980), *An Introduction to Atmospheric Physics*, 2nd ed., Academic Press, London.

Gassó, S. (2008), Satellite observations of the impact of weak volcanic activity on marine clouds, *J. Geophys. Res.*, *113*, D14S19, doi:10.1029/2007JD009106.

Han, Q. Y., W. B. Rossow, and A. A. Lacis (1994), Near-global survey of effective radii in liquid water clouds using ISCCP data, *J. Clim.*, *7*, 465–497, doi:10.1175/1520-0442(1994)007<0465:NGSOED>2.0.CO;2.

Harris, A., and M. Ripepe (2007), Temperature and dynamics of degassing at Stromboli, *J. Geophys. Res.*, *112*, B03205, doi:10.1029/2006JB004393.

Hergert, W., and T. Wriedt (2012), *The Mie Theory: Basics and Applications*, Springer Series in Optical Sciences, Berlin.

Jaupart, C., and S. Vergniolle (1988), Laboratory models of Hawaiian and Strombolian eruptions, *Nature*, *331*, 58–60, doi:10.1038/331058a0.

Jaupart, C., and S. Vergniolle (1989), The generation and collapse of a foam layer at the roof of a basaltic magma chamber, *J. Fluid Mech.*, *203*, 347–380, doi:10.1017/S0022112089001497.

Johnson, J., R. Aster, K. Jones, P. R. Kyle, and W. C. McIntosh (2008), Acoustic source characterization of impulsive Strombolian eruptions from the Mount Erebus lava lake, *J. Volcanol. Geotherm. Res.*, *177*, 673–686, doi:10.1016/j.jvolgeores.2008.06.028.

Kaulakys, B., V. Gontis, and M. Alaburda (2005), Point process model of 1/f noise vs a sum of Lorentzians, *Phys. Rev. E.*, *71*, 051105, doi:10.1103/PhysRevE.71.051105.

Koutsoyiannis, D. (2012), Clausius-Clapeyron equation and saturation vapour pressure: Simple theory reconciled with practice, *Eur. J. Phys.*, *33*, 295–305, doi:10.1088/0143-0807/33/2/295.

Lock, J. A., and L. Yang (1991), Mie theory model of the corona, *Appl. Opt.*, *30*, 3408–3414.

Lozano, A., H. Amaveda, F. Barreras, X. Jordà, and M. Lozano (2003), High-frequency ultrasonic atomization with pulsed excitation, *J. Fluids Eng.*, *125*, 941–945, doi:10.1115/1.1603301.

Matsushima, N. (2005), H_2O emission rate by the volcanic plume during the 2000–2002 Miyakejima volcanic activity, *Geophys. Res. Lett.*, *32*, L14307, doi:10.1029/2005GL023217.

Matsushima, N., and H. Shinohara (2006), Visible and invisible volcanic plumes, *Geophys. Res. Lett.*, *33*, L24309, doi:10.1029/2006GL026506.

McGonigle, A. J. S., and C. Oppenheimer (2003), Optical sensing of volcanic gas and aerosol emissions, in *Volcanic Degassing*, edited by C. Oppenheimer, D. M. Pyle, and J. Barclay, *Geol. Soc. London Spec. Publ.*, *213*, 149–168.

McGonigle, A. J. S., P. Delmelle, C. Oppenheimer, V. I. Tsanev, T. Delfosse, G. Williams-Jones, K. Horton, and T. A. Mather (2004), SO_2 depletion in tropospheric volcanic plumes, *Geophys. Res. Lett.*, *31*, L13201, doi:10.1029/2004GL019990.

Michaut, C., D. Bercovici, and R. S. J. Sparks (2009), Ascent and compaction of gas rich magma and the effects of hysteretic permeability, *Earth Planet. Sci. Lett.*, *282*, 258–267, doi:10.1016/j.epsl.2009.03.026.

Molina, I., A. Burgisser, and C. Oppenheimer (2012), Numerical simulations of convection in crystal-bearing magmas: A case study of the magmatic system at Erebus, Antarctica, *J. Geophys. Res.*, *117*, B07209, doi:10.1029/2011JB008760.

Oppenheimer, C., and P. R. Kyle (2008), Probing the magma plumbing of Erebus volcano, Antarctica, by open-path FTIR spectroscopy of gas emissions, *J. Volcanol. Geotherm. Res.*, *177*, 743–754, doi:10.1016/j.jvolgeores.2007.08.022.

Oppenheimer, C., A. S. Lomakina, P. R. Kyle, N. G. Kingsbury, and M. Boichu (2009), Pulsatory magma supply to a phonolite lava lake, *Earth Planet. Sci. Lett.*, *284*, 392–398, doi:10.1016/j.epsl.2009.04.043.

Patrick, M., D. Wilson, D. Fee, T. Orr, and D. Swanson (2011), Shallow degassing events as a trigger for very-long-period seismicity at Kīlauea Volcano, Hawai'i, *Bull. Volcanol.*, *73*, 1179–1186, doi:10.1007/s00445-011-0475-y.

Ripepe, M., A. J. L. Harris, and R. Carniel (2002), Thermal, seismic and infrasonic evidence of variable degassing rates at Stromboli volcano, *J. Volcanol. Geotherm. Res.*, *118*, 285–297, doi:10.1016/S0377-0273(02)00298-6.

Roehle, I., R. Schodl, P. Voigt, and C. Willert (2000), Recent developments and applications of quantitative laser light sheet measuring techniques in turbomachinery components, *Meas. Sci. Technol.*, *11*, 1023–1035, doi:10.1088/0957-0233/11/7/317.

Sawyer, G. M., G. G. Salerno, J. S. Le Blond, R. S. Martin, L. Spampinato, T. J. Roberts, T. A. Mather, M. L. I. Witt, V. I. Tsanev, and C. Oppenheimer (2011), Gas and aerosol emissions from Villarrica volcano, Chile, *J. Volcanol. Geotherm. Res.*, *203*, 62–75, doi:10.1016/j.jvolgeores.2011.04.003.

Shinohara, H. (2008), Excess degassing from volcanoes and its role on eruptive and intrusive activity, *Rev. Geophys.*, *46*, RG4005, doi:10.1029/2007RG000244.

Siebert, L., T. Simkin, and P. Kimberly (2010), *Volcanoes of the World*, 3rd ed., Univ. of California Press, Berkeley.

Sigurdsson, H., B. Houghton, H. Rymer, J. Stix, and S. McNutt (1999), *Encyclopedia of Volcanoes*, 1st ed., Academic Press, San Francisco, Calif.

Suzuki, Y. J., and T. Koyaguchi (2010), Numerical determination of the efficiency of entrainment in volcanic eruption columns, *Geophys. Res. Lett.*, *37*, L05302, doi:10.1029/2009GL042159.

Sweeney, D., P. R. Kyle, and C. Oppenheimer (2008), Sulfur dioxide emissions and degassing behavior of Erebus volcano, Antarctica, *J. Volcanol. Geotherm. Res.*, *177*, 725–733, doi:10.1016/j.jvolgeores.2008.01.024.

Symonds, R. B., W. I. Rose, G. J. S. Bluth, and T. M. Gerlach (1994), Volcanic-gas studies: Methods, results, and applications, in *Volatiles in Magmas*, *Rev. Mineral.*, vol. 30, edited by M. R. Carroll and J. R. Holloway, pp. 1–66, Mineralogical Society of America, Washington, D. C.

Tamburello, G., A. Aiuppa, E. P. Kantzas, A. J. S. McGonigle, and M. Ripepe (2012), Passive vs. active degassing modes at an open-vent volcano (Stromboli, Italy), *Earth Planet. Sci. Lett.*, *359*, 106–116, doi:10.1016/j.epsl.2012.09.050.

Tamburello, G., A. Aiuppa, A. J. S. McGonigle, P. Allard, A. Cannata, G. Giudice, E. P. Kantzas, and T. D. Pering (2013), Periodic volcanic degassing behavior: The Mount Etna example, *Geophys. Res. Lett.*, *40*, 4818–4822, doi:10.1002/grl.50924.

Terhaar, S., and C. O. Paschereit (2012), High-speed PIV investigation of coherent structures in a swirl-stabilized combustor operating at dry and steam-diluted conditions, paper presented at 16th Int. Symp. on Applications of Laser Techniques to Fluid Mechanics, Lisbon, Portugal.

Turcotte, D. L. (1999), Self-organized criticality, *Rep. Prog. Phys.*, *62*, 1377–1429, doi:10.1088/0034-4885/62/10/201.

Witter, J. B., P. Hernández, A. J. L. Harris, and N. Pérez (2012), Quantification of the mass flux of H_2O gas (steam) at three active volcanoes using thermal infrared imagery, *Pure Appl. Geophys.*, *169*, 1875–1889, doi:10.1007/s00024-011-0446-4.

Wüller, D., and H. Gabele (2007), The usage of digital cameras as luminance meters, *Proc. SPIE*, *6502*, U5020.

Yano, J. I., R. Blender, C. Zhang, and K. Fraedrich (2004), 1/f noise and pulse-like events in the tropical atmospheric surface variabilities, *Q. J. R. Meteorol. Soc.*, *130*, 1697–1721, doi:10.1256/qj.03.42.

Zimmer, M., and J. Erzinger (2003), Continuous H_2O, CO_2, ^{222}Rn and temperature measurements on Merapi volcano, Indonesia, *J. Volcanol. Geotherm. Res.*, *125*, 25–38, doi:10.1016/S0377-0273(03)00087-8.

Zuidema, P., and D. L. Harunann (1995), Satellite determination of stratus cloud microphysical properties, *J. Clim.*, *8*, 1638–1656, doi:10.1175/1520-0442(1995)008<1638:SDOSCM>2.0.CO;2.